Supporting Information

Maurer et al. 10.1073/pnas.1116510109

SI Discussion

Our Ras-binding compounds act as inhibitors of SOS-mediated nucleotide exchange. We predict that inhibition of Ras nucleotide exchange will provide therapeutic benefits both for Ras wild-type tumors as well as for some Ras mutant tumors.

Ras exchange inhibitors are expected to be efficacious in Ras wild-type tumors that are dependent on Ras signaling, such as tumors with constitutive activation of EGF receptor (EGFR), with human epidermal growth factor receptor amplification, or with neurofibromin 1 inactivating mutations. More importantly, these inhibitors are expected to have great therapeutic benefits when combined with other Ras pathway inhibitors, such as a mitogen-activated protein kinase kinase (MEK) inhibitor. MEK inhibition alone is not effective in inhibiting the proliferation of Ras wild-type cells (1). We speculate that the MEK-mediated negative feedback contributes to this lack of response. MEK activates ERK, which, in turn, directly phosphorylates SOS and inhibits its nucleotide exchange activity, thereby down-regulating the Ras^{GTP} level in wild-type cells (2–4). Inhibition of MEK by MEK inhibitors abolishes this negative feedback and up-regulates the Ras^{GTP} level in Ras wild-type cells (5, 6), leading to hyperactivation of Ras signaling to PI3K, Ral guanine nucleotide dissociation stimulator, etc. Thus, a combination of MEK inhibitors and an exchange inhibitor is expected to be more efficacious than MEK inhibitors alone. The relevance of targeting SOS [and other Ras guanine nucleotide exchange factors (GEFs)] in mutant Ras tumors is less well characterized. Initial experiments showed that sequestration of Ras GEFs by overexpression of HRasS17N (which preferentially binds GDP) prevented the transformed phenotype of NIH 3T3 cells overexpressing wild-type, but not mutant HRas (7). Similarly, SOS1-null embryonic fibroblasts allowed transformation by overexpression of mutant KRas, but not upstream oncogenic regulators such as EGFR or viral-sarcoma (8). However, these experiments have generally been performed using gene overexpression in unphysiological model systems. In contrast to the concept that overexpressed mutant Ras is insensitive to SOS inhibition, literature reports demonstrate that under physiological conditions, mutant Ras-expressing cells require signaling through WT Ras isoforms to elicit transformation. For example, in many mutant Ras models, activation of the MAP kinase pathway remains dependent on growth factor signaling (9–12). Similarly, in two independent mutant KRas pancreatic tumor models, both mutant KRas and wild-type HRas are required for tumor growth in vivo (13). Because different Ras isoforms signal to different downstream effector pathways to mediate diverse physiological/pathological functions (14–16), we speculate that this codependence between the mutant and wild-type Ras isoforms results from differential signaling by respective Ras isoforms, the sum of which is required for transformation. Although mutant Ras is less or may not be dependent on Ras GEFs for maintaining its high Ras^{GTP} levels, this codependence of mutant and wild-type Ras isoforms suggests a requirement of Ras GEFs in transformation and points to a possible therapeutic efficacy by inhibition of Ras GEFs in Ras-driven tumors. Unlike in the nontransformed cells in which activation of SOS is dependent on growth factor signaling, SOS in mutant Ras tumors may become constitutively active due to the high level of mutant Ras^{GTP} that allosterically activates SOS (17), which, in turn, activates wild-type Ras isoforms required for transformation. This differential activation mechanism provides a potential therapeutic window for targeting SOS in Ras-driven tumors.

SI Materials and Methods.

Molecular Cloning and Protein Purification. Sequence encoding full-length human KRas4B (amino acids 1–188) was amplified by PCR and subcloned into a modified pET-52b expression vector (Novagen) for expression in *Escherichia coli*. Individual point mutations, G12D and R41S, were introduced by site-directed mutagenesis (QuikChange; Agilent Technology). The KRas4B-G12D mutant was referred to as $KRas_m$ throughout the paper. Sequence encoding the Ras exchanger motif and Cdc25 domains of human SOS1 (amino acids 564–1049) was amplified by PCR and subcloned into a modified pAcGP67a expression vector (Pharmingen) for expression in insect cells and in *E. coli*. The identity of all expression constructs were confirmed by DNA sequencing.

For structural studies, the N-terminal His-tagged $KRas_m$ construct was transformed into BL21(DE3) cells. Cells were grown at 37 °C to an absorbance of 0.5 (OD_{600}) in LB media containing 50 μg/mL of carbenicillin and then transferred to 20 °C prior to induction with 0.5 mM IPTG at an absorbance of 0.8 (OD_{600}). Cells were harvested 12 h after induction and the pellet was lysed by passing through a microfluidizer in a buffer containing 50 mM TrisCl, pH 8.0, 500 mM NaCl, 0.5% Triton X-100, 5 mM MgCl2, and EDTA-free protease inhibitor tablets (Roche). Cell lysates were loaded onto a HisTrap HP column (GE Healthcare) in a buffer containing 50 mM TrisCl, pH 8.0, 500 mM NaCl, and 5 mM $MgCl_2$ and the bound $KRas_m$ protein was eluted with 200 mM imidazole in the same buffer. The N-terminal His-tag was cleaved by the tobacco etch virus protease and removed using a nickel column. The $KRas_m$ protein was further purified on a size-exclusion Superdex 75 column (GE Healthcare) in a buffer containing 25 mM TrisCl, pH 8.0, 100 mM NaCl, 5 mM $MgCl_2$, and 1 mM tris(2-carboxyethyl)phosphine (TCEP). Fractions containing $KRas_m$ were collected, concentrated to 10 mg/mL, frozen, and stored at −80 °C. The purity of $KRas_m$ was greater than 95% as assayed by SDS-PAGE.

For enzymatic studies, N-terminal His-tagged full-length KRas4B (wild type, G12D, or R41S) constructs were transformed into BL21(DE3) cells. Cells were grown at 37 °C to an absorbance of 0.5 (OD_{600}) in Terrific Broth media containing 50 μg/mL of carbenicillin and then transferred to 20 °C prior to induction with 1 mM IPTG at an absorbance of 1.0 (OD_{600}). Cells were harvested 16 h after induction and the KRas proteins were purified from cell lysates as described above, except that the N-terminal His-tag was not removed.

For the binding assays, an N-terminal His-Avi-tagged full-length KRas4B construct was cotransformed with a vector expressing the *E. coli* biotin ligase (BirA) into BL21(DE3) cells for expression and in vivo biotinylation of KRas4B using AviTag™ technology (Avidity) (18). Protein was expressed and purified as described above.

Uniformly ^{15}N-labeled N-terminal His-tagged full-length $KRas_m$ was produced in BL21(DE3) cells. Colonies from an agar plate were used to inoculate 25 mL of labeled M9 medium plus $^{15}NH_4Cl$ as the sole nitrogen source and cultured overnight at 37 °C. The culture was then used to inoculate in 1 L of the minimal medium containing 2 mL 2 M $MgSO_4 \cdot 7H_2O$ (0.26 g/L), 50 mL 20xM9 salts (depleted of nitrogen), 1 mL vitamin solution (R7256; Sigma), 0.1 mL trace elements, and 1 g of ^{15}N Isogro (606839-SPEC; Sigma). The culture was grown at 37 °C until cells had reached an absorbance of 0.6–0.8 (OD_{600}), and then

transferred to 20 °C, followed by induction with 1 mM IPTG for 16 h.

For expression of recombinant SOS^{cat} in insect cells, the N-terminal His-tagged SOS^{cat} construct was cotransfected into *Sf9* cells with BaculoGold linearized baculoviral DNA (BD Biosciences) and the initial viral supernatant was amplified twice to generate recombinant viral stocks. *Tni* PRO (Expression Systems) cells were grown to a density of 2 × 106 cells/mL in ESF921 media (Expression Systems) and infected with a high-titer viral stock at a ratio of 5 mL/L (moi = 1). Cells were harvested after 48 h by centrifugation and frozen at −80 °C. Cell lysates were loaded onto a Ni-nitrilotriacetate Superflow column (Qiagen) in a buffer containing 50 mM TrisCl, pH 8.0, 500 mM NaCl, and 5 mM $MgCl_2$ and bound SOS^{cat} protein was eluted with 200 mM imidazole in the same buffer. The SOS^{cat} protein was further purified by a size-exclusion Superdex 75 column (GE Healthcare) in a buffer containing 25 mM TrisCl, pH 7.5, 150 mM NaCl, 5 mM $MgCl_2$, and 0.5 mM TCEP. Fractions containing SOS^{cat} were collected, frozen, and stored at −80 °C. The purity of the SOS^{cat} protein was greater than 95% as assayed by mass spectrometry and by SDS-PAGE with Coomassie brilliant blue staining.

Nucleotide Loading onto the KRas Proteins. To load guanosine-5′-[(β, γ)-methyleno]triphosphate (GMPPCP) on $KRas_m$ used in the structural studies, purified $KRas_m$ (in a mixed population of GDP and GTP states) was first incubated with 40 mM EDTA plus 2 mM GMPPCP (Sigma) at 20 °C, then exchanged by a NAP-5 column (GE Healthcare) into an EDTA-free and MgCl2-free buffer containing 32 mM TrisCl, pH 8.0, 200 mM $(NH_4)_2SO_4$, and 0.1 mM $ZnCl_2$. Alkaline phosphatase agarose (Sigma) was added at 4 units per milligram of $KRas_m$ and incubated overnight at 4 °C. The phosphatase agarose beads were then removed and 40 mM $MgCl_2$ was added to $KRas_m$, which was subsequently dialyzed into a nucleotide-free buffer. To load GDP, purified KRas was incubated with 40 mM EDTA plus 2 mM GDP at 20 °C. Subsequently, 80 mM $MgCl_2$ was added to KRas and the reaction mix was then dialyzed into a nucleotide-free buffer.

To load *N*-methylanthraniloyl (MANT)-GDP, MANT-5′-guanylyl imidodiphosphate (GMPPNP), or GDP onto KRas for enzymatic studies, purified KRas (wild type, G12D, or R41S) was first buffer-exchanged by a NAP-5 column (GE Healthcare) into a low Mg^{2+} buffer (20 mM TrisCl, pH 7.5, 50 mM NaCl, and 0.5 mM $MgCl_2$). The KRas protein was then incubated with a 20-fold molar excess of MANT-GDP (Invitrogen), MANT-GMPPNP (Invitrogen), or GDP (Sigma) in the presence of 5 mM EDTA and 1 mM DTT for 1.5 h at 20 °C. The reactions were then supplemented with 10 mM MgCl2 and incubated for 30 min at 20 °C. The free nucleotides were removed by gel filtration using a PD-10 column (GE Healthcare) that had been equilibrated in the reaction buffer (40 mM Hepes-KOH, pH 7.5, 10 mM $MgCl_2$ and 1 mM DTT). The percent of KRas bound by fluorescent nucleotide was determined against a standard curve of MANT-GDP or MANT-GMPPNP.

Fragment Screening and Hit Validation. Compounds in the fragment library screened were selected from commercial sources. Criteria for selection were 16 or fewer non-hydrogen atoms, a cLogP less than three, and not containing potentially reactive functional groups. All fragments were analyzed by NMR for their structural integrity and solubility. For saturation transfer difference (STD) experiments, presaturation was achieved using a pulse train of 30 ms Gaussian shaped pulses for a 3-s duration and an offset of −1 ppm (on resonance) or −60 ppm (off resonance). To obtain STD spectra, 128 on and off resonance of free induction decays were recorded. Subtraction of the on-resonance from the off-resonance spectra yielded the STD signal. Compounds with STD signal-to-noise ratio greater than five were remeasured as individual compounds for binding to $KRas_m{}^{GDP}$ or $KRas_m{}^{GMPPCP}$ separately.

Hits were further tested for specific binding to $KRas_m$ by measurement of ^1H ^{15}N heteronuclear single quantum coherence (HSQC) protein spectra. Positive hits were defined as compounds that exhibit cross-peak perturbation by more than 15 Hz (combined ^{15}N and ^1H chemical shift change) when compared to the spectrum recorded in the absence of compounds. Compound stocks were prepared in DMSO solution. Therefore, we measured the protein spectrum in the presence of DMSO without compound as a background control to identify chemical shift perturbations induced by DMSO. The majority of perturbations not labeled in Fig. S1*C* result from this DMSO effect. All data were collected using a Tokyo Chemical Industry 5-mm cryoprobe and spectrometers running at 500 and 600 MHz. ^1H ^{15}N HSQC spectra were recorded with 32 transients and 192 data points in the indirect dimension.

Our confirmed hits have diverse chemical structures. Twenty-four out of the 25 hits contain aromatic heterocycles with two rings that are fused (six hits), directly linked (six hits), or linked via one or two linker atoms (11 hits). The fused heterocycles consist of indoles, indazoles, or benzimidazoles, and this group exhibits the greatest NMR shifts within the hit set. Average molecular mass of the hits is 187, with a range from 134 to 240 Da.

K_d Measurement by NMR Assays. K_d values were determined by recording a series of ^{15}N HSQC spectra with an increasing ligand concentration. The chemical shift changes were determined in units of ppm through multiplication of the respective ^{15}N and ^1H Hz shifts by a correction factor of 1.44 for ^1H and 0.23 for ^{15}N (19). The calculated ppm values were plotted as a function of ligand concentration. For 4,6-dichloro-2-methyl-3-aminoethylindole (DCAI) and benzimidazole (BZIM), spectra with ligand concentrations of 0, 250, 500, 1,000, 2,000, and 4,000 μM were recorded. The curves were fit to an exponential function. Reported K_d values were based on the average of values obtained from the fit for residues T74 and G75 for DCAI and BZIM, and additionally L56 for DCAI, which showed no analyzable shift with BZIM.

Crystallization, Data Collection, and Structure Determination. Diffraction quality crystals were grown at 4 °C from 0.2 ± 0.2 μL vapor diffusion drops containing 40 mg/mL $KRas_m$, 0.1 M TrisCl, pH 8.5, 25% polyethylene glycol 4,000, 0.2 M NaOAc, and 2% benzamidine-HCl. Crystals appeared in 2 wk and typically grew to 30 × 70 × 30 μm^3. For data collection, crystals were harvested with 10% glycerol in the crystallization solution. For crystal soaking, the confirmed fragment hits were soaked as individual compounds at a concentration of 100 mM. Fragment soaking solutions were made in 20 mM TrisCl, pH 8.0, 30% polyethylene glycol 4,000, and 0.2 M NaOAc. The high compound concentration was necessary to yield well-defined electron density maps. Crystals were transferred into the soaking solution and incubated overnight at 4 °C. The diffraction data were collected under cryogenic temperature at synchrotron radiation sources and detectors as indicated in Table S1.

The diffraction datasets were indexed, integrated, and scaled using the program HKL2000 (20). The data processing statistics are shown in Table S1. The structure of $KRas_m$ was solved by molecular replacement method using the program Phaser (21). The HRas structure (Protein Data Bank code 2Q21) was used as an initial molecular replacement search model. Residues in the C-terminal domain (residues 170–180) were built based on the difference map. Switch regions were variable and required additional model building. Manual model rebuilding was done with the program COOT (22). Structure refinement was carried out iteratively with the program REFMAC5 (23) and PHENIX (24), using the maximum likelihood target functions, anisotropic indi-

vidual B-factor refinement, and translation/libration/screw refinement, to achieve the final R factors shown in Table S1. To determine the ligand-bound structures, the refined KRas structure of the corresponding nucleotide state was initially subjected to rigid body refinement and positional refinement. Manual inspection of the difference maps ($F_o - F_c$ and $2F_o - F_c$) identified ligand binding. The ligand structures and the surrounding residues of the protein were built according to the electron density map. The ligand-$KRas_m$ structure was then refined to R factor reaching convergence in a similar manner as described above (Table S1). BZDN was used as a crystallization agent. The location of the benzamidine (BZDN)-binding site is in the vicinity of the crystal packing interface, and BZDN appears to interact with the neighboring Ras molecule. However, crystals could form in identical space group and unit cell in the absence of BZDN. BZIM and DCAI bind to the identical site of Ras but do not directly interact with the crystallographic neighboring Ras molecule. Hence we concluded that the complex structures likely represent the ligand-binding mode in solution.

Crystal soaking resulted in costructures of BZIM bound to $KRas_m{}^{GDP}$ only and of DCAI bound to $KRas_m{}^{GMPPCP}$ only, whereas NMR measurements indicated that these compounds bind to both nucleotide-bound states. BZDN was present in both nucleotide states of the $KRas_m$ crystals. This apparent selectivity for a particular nucleotide state in crystallography may reflect a difference of binding affinity. A confounding factor may be the difference between the conditions used in NMR versus crystallography experiments.

Guanine Nucleotide Exchange Assays. Nucleotide exchange rates were measured by incubation of 500 nM $KRas^{GDP}$ in a buffer containing 40 mM Hepes-KOH, pH 7.5, 10 mM $MgCl_2$, and 1 mM DTT and 500-nM-labeled MANT-GMPPNP. The SOS^{cat}-catalyzed nucleotide exchange was then initiated by addition of recombinant His-tagged SOS^{cat} to a final concentration of 250 nM, unless otherwise specified. Nucleotide release rates were measured by the incubation of 125 nM $KRas^{MANT\text{-}GDP}$ in a buffer containing 40 mM Hepes-KOH, pH 7.5, 10 mM $MgCl_2$, and 1 mM DTT and 200 μM unlabeled GMPPNP. The SOS^{cat}-catalyzed nucleotide release reactions were initiated by addition of 125 nM SOS^{cat}, unless otherwise specified. The EDTA-mediated nucleotide release reactions were initiated by the addition of 20 mM EDTA. For intrinsic nucleotide release assays, $KRas_m{}^{MANT\text{-}GMPPNP}$ was incubated in the reaction buffer and monitored after addition of 200 μM unlabeled GMPPNP. For all exchange assays with compounds, reactions were incubated either with DMSO or with indicated compounds (final concentration of DMSO of 0.5%) for 5 min prior to the addition of SOS^{cat} or nucleotide.

In the exchange assays shown in Fig. 3*D*, reactions were performed as above with 500 nM of $KRas^{GDP}$, $RhoA^{GDP}$, or $Cdc42^{GDP}$, and exchange was initiated by the addition of SOS^{cat} or Dbs (Cytoskeleton) to a final concentration of 800 nM. The higher concentration of GEFs was chosen here to provide the optimal assay window for these three reactions.

Comparison of DCAI-induced inhibition of nucleotide release of KRas and $KRas_m$ are shown in Fig. 3*C*. These reactions were performed as described above, except that 500 nM SOS^{cat} was used to catalyze the reaction. This concentration of SOS^{cat} was chosen because it provided the optimal assay window for KRas and $KRas_m$.

For all exchange assays, changes in fluorescence were measured by a fluorescence spectrometer (Envision model 2103; Perkin Elmer) in a black 96 half-area well plate (Corning 3686). Fluorescence was excited at $\lambda = 370$ nm and emission was monitored at $\lambda = 450$ nm every 20 s for over 30 min at 20 °C. The data were then normalized to the mean fluorescence per well prior to enzyme addition, normalized to "no SOS" control at $t = 100$ s to allow for any small disturbances in fluorescence to settle, and then fit to a single exponential decay or association function using the program Prism (GraphPad Software). The derived rates were normalized against that of the DMSO-treated samples and plotted against compound concentration as mean ± SEM. The IC_{50} for each compound was calculated by plotting the normalized rates against the log of compound concentration, and then fit to a four-parameter dose-response curve using Prism.

Statistical Analyses. Statistical significance of exchange rate data presented as the mean normalized rate ± SEM was analyzed by Student's *t* test against DMSO control. A *p* value below 0.005 was considered to be statistically significant.

KRas-SOS Binding Assays. His6-SOS^{cat} recombinant protein (at 100 nM) was briefly incubated with 100 nM of biotinylated His_6-Avi-KRas in 200 μL of a binding buffer consisting of 20 mM Hepes-KOH, pH 7.5, 50 mM NaCl, 1 mM DTT, 0.1% BSA, and 0.03% Tween 20 plus either 5 mM EDTA (+EDTA) or 10 mM MgCl2 (−EDTA). The test compounds were incubated with KRas for 5 min prior to the addition of His_6-SOS^{cat}. Following incubation at 20 °C for 30 min under constant agitation, 10 μL of Streptavidin M1 Dynabeads (Invitrogen) that had been prewashed in the binding buffer were added to each reaction. Samples were incubated for an additional 15 min at 20 °C. The beads were then purified, washed five times with the binding buffer, and resuspended in the SDS-PAGE sample buffer. Bound proteins were then separated by SDS-PAGE and the amounts of KRas and SOS were detected by anti-His Western blotting and quantified using an infrared imaging system (Odyssey; Li-Cor). Changes in the binding efficiency with increasing compound dose were calculated by normalizing to the level of KRas and then to DMSO-treated samples.

Assays for Measuring Endogenous Ras^{GTP} Levels. Levels of endogenous Ras^{GTP} were determined by a GST-tagged Ras-binding domain (RBD) effector pull-down assay (Thermo Scientific). HEK 293T cells were grown to log phase and then serum-starved for 16 h before compound addition. After a 4-h incubation with compounds, cells were then treated with 100 ng/mL of EGF for 5 min before lysis in Cell Lysis Buffer (Thermo Scientific). Lysates were clarified, protein concentrations normalized, and then levels of the endogenous GTP-bound Ras in lysates were measured by an effector pull-down assay per manufacture's instruction (Thermo Scientific).

Cellular RBD-Cysteine-Rich Domain (CRD) Redistribution Assays. HEK 293 T-REx Flp-In cells inducibly expressing Venus-RBD-CRD/mCherry-CAAX or Venus-Smad7/Smurf1-eCFP were generated by targeted integration (Invitrogen). Expression of fluorescent fusion proteins were induced with 1 μg/mL Doxycycline for 24 h in 384-well plates and cells were imaged with a Nikon Ti-perfect focus A1R inverted confocal microscope as described previously (5). Compounds were added 100 min after first frame of acquisition and cells were imaged 20 min after compound addition and then every subsequent 2 h. Image acquisition and quantification of plasma-membrane-associated Venus-RBD-CRD or Venus-Smad7 were conducted as described (5). Briefly, local pixel intensities dividing plasma membrane localized Venus-RBD-CRD signal by cytoplasmic Venus-RBD-CRD signal were measured radially around the plasma membrane within every cell in an image. These ratios of Venus-RBD-CRD plasma membrane to cytoplasmic targeting were then averaged for each condition. Membrane targeting ratios were subtracted from time zero and dose curve data was fit to sigmoidal curves to calculate EC_{50}. Plasma membrane was visualized and masked using mCherry fused to the amino terminus of the CAAX motif of KRas (5).

Quantification of Cellular Concentrations of Ras and SOS1 by Western Blotting. HEK 293T cells were lysed in the RIPA buffer (0.15 mM NaCl/0.05 mM Tris·HCl, pH 7.2/1% Triton X-100/1% sodium deoxycholate/0.1% SDS) and whole cell lysates were probed with a pan-Ras antibody (EP1125Y) (Abcam) and an SOS1 antibody (raised and affinity-purified against recombinant $SOS1_{564–1049}$). The amounts of Ras and SOS1 in the lysates were quantified using an infrared imaging system (Odyssey; Li-Cor). Intensity values were normalized to a standard curve of recombinant proteins and cellular concentrations of Ras and SOS1 estimated.

1. Solit DB, et al. (2006) BRAF mutation predicts sensitivity to MEK inhibition. *Nature* 439:358–362.
2. Buday L, Warne PH, Downward J (1995) Down-regulation of the Ras activation pathway by MAP kinase phosphorylation of Sos. *Oncogene* 11:1327–1331.
3. Dong C, Waters SB, Holt KH, Pessin JE (1996) SOS phosphorylation and disassociation of the Grb2-SOS complex by the ERK and JNK signaling pathways. *J Biol Chem* 271:6328–6332.
4. Porfiri E, McCormick F (1996) Regulation of epidermal growth factor receptor signaling by phosphorylation of the ras exchange factor hSOS1. *J Biol Chem* 271:5871–5877.
5. Anderson DJ, et al. (2011) Live-cell microscopy reveals small molecule inhibitor effects on MAPK pathway dynamics. *PloS One* 6:e22607.
6. Kamioka Y, Yasuda S, Fujita Y, Aoki K, Matsuda M (2010) Multiple decisive phosphorylation sites for the negative feedback regulation of SOS1 via ERK. *J Biol Chem* 285:33540–33548.
7. Feig LA, Cooper GM (1988) Inhibition of NIH 3T3 cell proliferation by a mutant ras protein with preferential affinity for GDP. *Mol Cell Biol* 8:3235–3243.
8. Qian X (2000) The Sos1 and Sos2 Ras-specific exchange factors: Differences in placental expression and signaling properties. *EMBO J* 19:642–654.
9. Kim JS, Lee C, Foxworth A, Waldman T (2004) B-Raf is dispensable for K-Ras-mediated oncogenesis in human cancer cells. *Cancer Res* 64:1932–1937.
10. Tuveson DA (2004) Endogenous oncogenic K-ras(G12D) stimulates proliferation and widespread neoplastic and developmental defects. *Cancer Cell* 5:375–387.
11. Li Q (2010) Hematopoiesis and leukemogenesis in mice expressing oncogenic NrasG12D from the endogenous locus. *Blood* 117:2022–2032.
12. Hamilton M, Wolfman A (1998) Oncogenic Ha–Ras–dependent mitogen–activated protein kinase activity requires signaling through the epidermal growth factor receptor. *J Biol Chem* 273:28155–28162.
13. Lim KH, Ancrile BB, Kashatus DF, Counter CM (2008) Tumour maintenance is mediated by eNOS. *Nature* 452:646–649.
14. Fotiadou PP, Takahashi C, Rajabi HN, Ewen ME (2007) Wild-type NRas and KRas perform distinct functions during transformation. *Mol Cell Biol* 27:6742–6755.
15. Voice JK, Klemke RL, Le A, Jackson JH (1999) Four human ras homologs differ in their abilities to activate Raf-1, induce transformation, and stimulate cell motility. *J Biol Chem* 274:17164–17170.
16. Yan J, Roy S, Apolloni A, Lane A, Hancock JF (1998) Ras isoforms vary in their ability to activate Raf-1 and phosphoinositide 3-kinase. *J Biol Chem* 273:24052–24056.
17. Margarit SM, et al. (2003) Structural evidence for feedback activation by Ras.GTP of the Ras-specific nucleotide exchange factor SOS. *Cell* 112:685–695.
18. Cull MG, Schatz PJ (2000) Biotinylation of proteins in vivo and in vitro using small peptide tags. *Methods Enzymol* 326:430–440.
19. Schumann FH, et al. (2007) Combined chemical shift changes and amino acid specific chemical shift mapping of protein–protein interactions. *J Biomol NMR* 39:275–289.
20. Otwinowski Z, Minor V (1997) Processing of X-ray diffraction data collected in oscillation mode. *Methods Enzymol* 276:307–326.
21. McCoy AJ, et al. (2007) Phaser crystallographic software. *J Appl Crystallogr* 40:658–674.
22. Emsley P, Cowtan K (2004) Coot: Model-building tools for molecular graphics. *Acta Crystallogr D Biol Crystallogr* 60:2126–2132.
23. Murshudov GN, Vagin AA, Dodson EJ (1997) Refinement of macromolecular structures by the maximum-likelihood method. *Acta Crystallogr D Biol Crystallogr* 53:240–255.
24. Adams PD, et al. (2010) PHENIX: A comprehensive Python-based system for macromolecular structure solution. *Acta Crystallogr D Biol Crystallogr* 66:213–221.

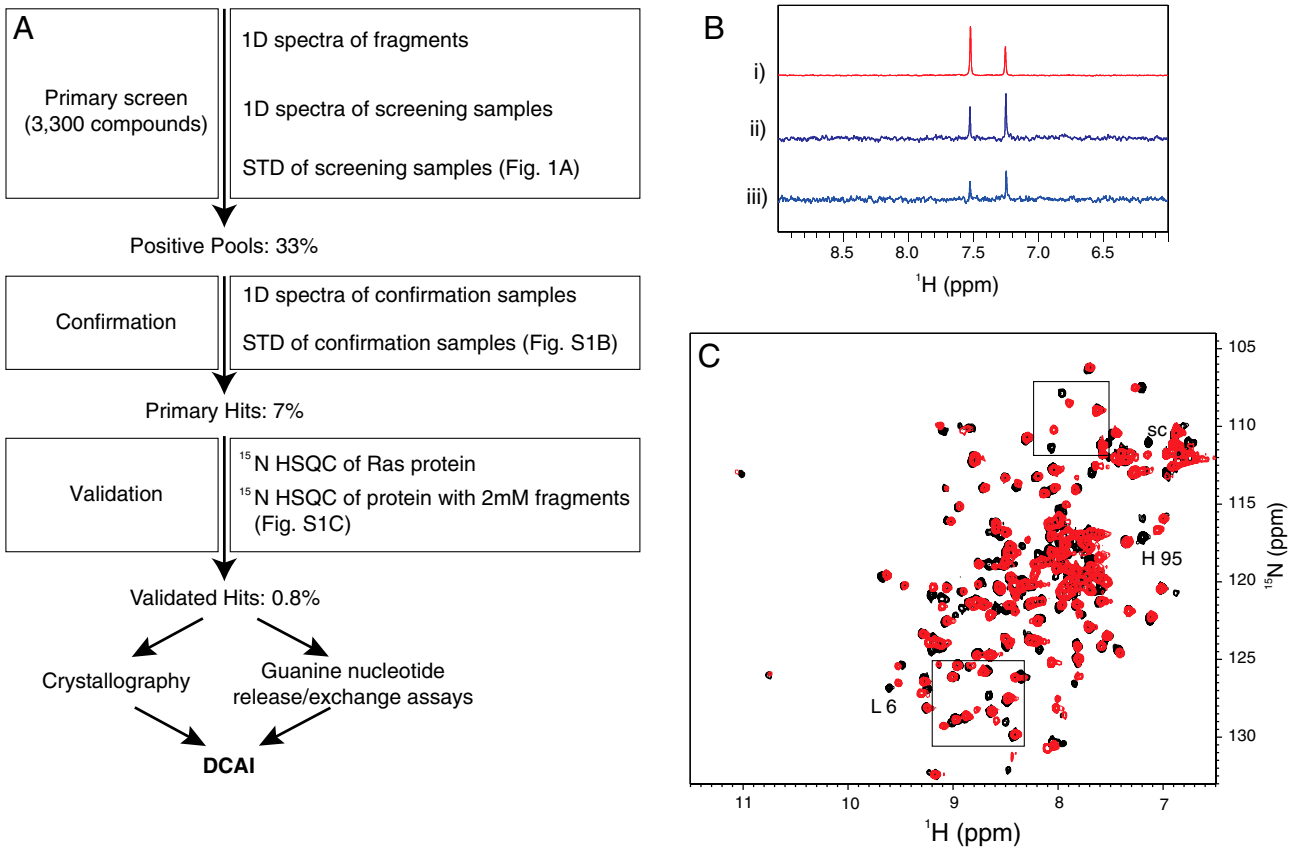

Fig. S1. Identification of DCAI. (*A*) The NMR-based screening and validation workflow. (*B*) One-dimensional proton spectra showing representative NMR confirmation results. (*i*) The 1D reference spectrum of DCAI as a single compound. (*ii*) The STD spectrum of DCAI as a single compound with 5 μM $KRas_m^{GMPPCP}$. (*iii*) The STD spectrum of DCAI as a single compound with 5 μM $KRas_m^{GDP}$. (*C*) Shown is the ^1H ^{15}N HSQC of $KRas_m^{GDP}$ at 100 μM concentration with (red) or without (black) 2 mM DCAI. The boxed-area spectra of $KRas_m^{GDP}$ are shown in Fig. 1*B*. DMSO and pH changes also induced chemical shift perturbations. The majority of unlabeled perturbations outside of the boxed regions in the spectra resulted from this DMSO/pH effect (see *SI Materials and Methods*).

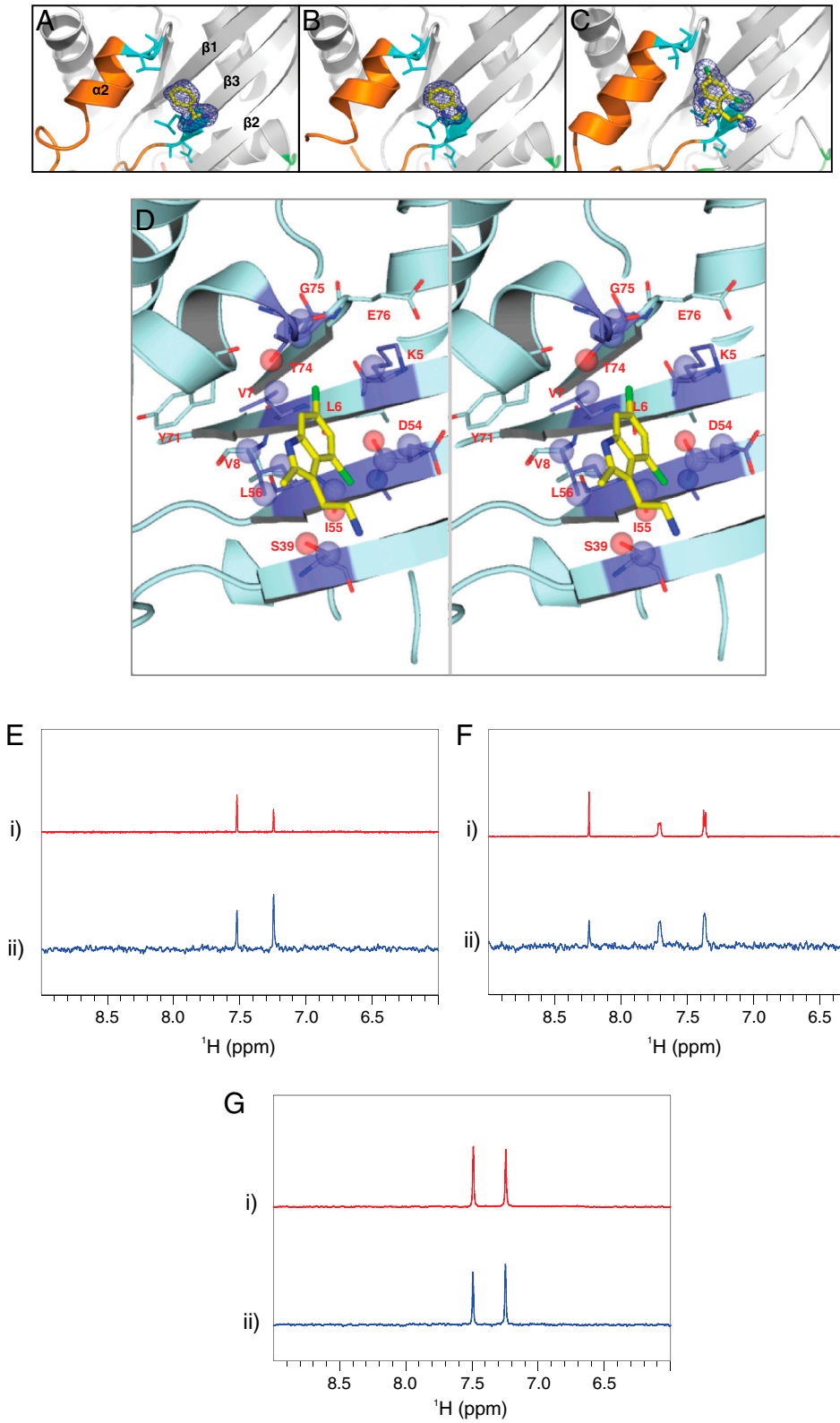

Fig. S2. Interactions between Ras and small-molecule binders. (*A–C*) Electron density of compounds bound to $KRas_m$ shown in blue mesh: (*B*) BZDN-$KRas_m^{GTP\gamma S}$, (*C*) BZIM-$KRas_m^{GDP}$, and (*D*) DCAI-$KRas_m^{GMPPCP}$. (*D*) Interactions between DCAI and KRas. A close-up stereoview (wall-eyed) of DCAI binding pocket in $KRas_m^{GTP}$. Residues directly interacting with DCAI are colored in darker blue. Spheres indicate atoms within 4 Å from DCAI. (*E*) DCAI binds to $HRas^{GDP}$. (*i*) The 1D proton reference spectrum of DCAI. (*ii*) The STD spectrum of DCAI incubated with $HRas^{GDP}$. (*F*) BZIM binds to $HRas^{GDP}$. (*i*) The 1D proton reference spectrum of BZIM. (*ii*) The STD spectrum of BZIM incubated with $HRas^{GDP}$. (*G*) DCAI binds to KRas-K41S^{GDP}. (*i*) The 1D proton reference spectrum of DCAI. (*ii*) The STD spectrum of DCAI incubated with KRas-K41S^{GDP}.

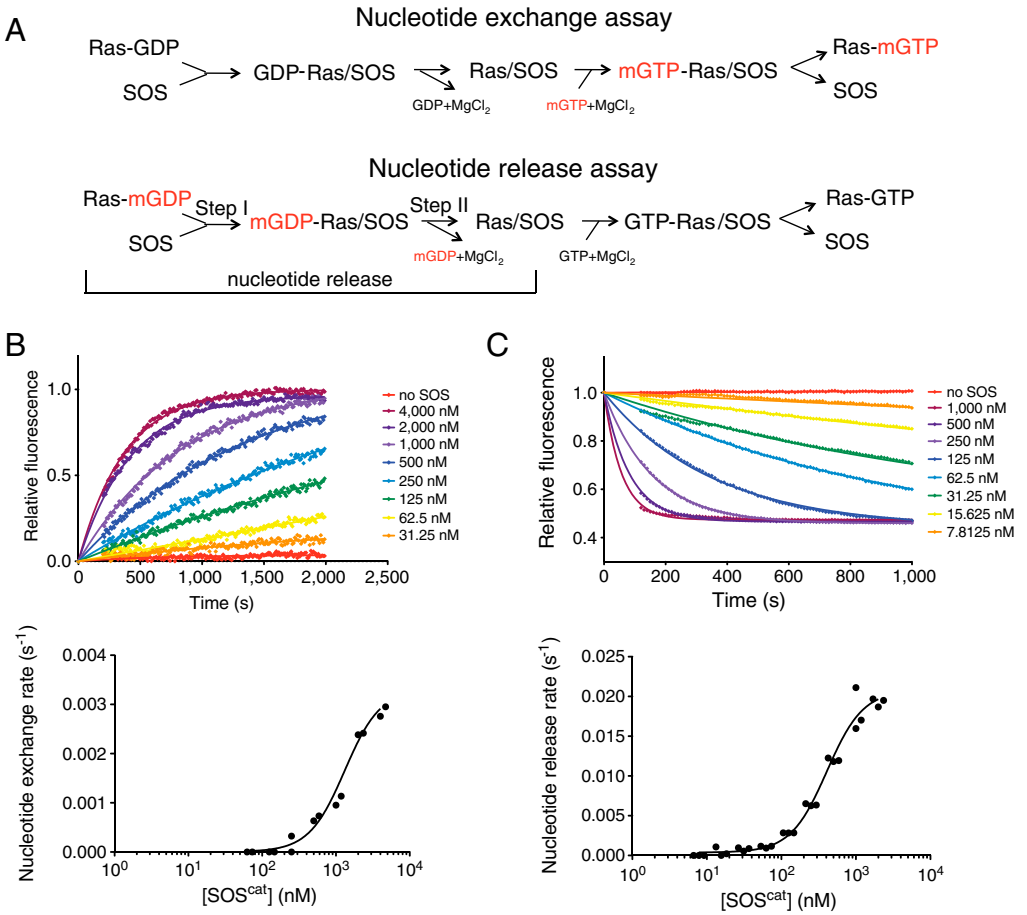

Fig. S3. Enzymatic characterization of the SOS^{cat}-catalyzed nucleotide exchange/release. (*A*) Schematics of the nucleotide exchange and release reactions. (*Upper*) The nucleotide exchange assay measures the exchange between free MANT-GMPPNP and KRas-bound GDP. This assay monitors the entire exchange reaction and can detect perturbations to all four diagrammed steps of SOS^{cat}-catalyzed exchange reaction. (*Lower*) The nucleotide release assay measures the release of MANT-GDP from $KRas^{MANT\text{-}GDP}$. This assay directly monitors the initial two steps of the SOS^{cat}-catalyzed reaction: formation of the Ras^{GDP}-SOS complex, followed by nucleotide release (1). At the low Ras and SOS protein concentrations used in our assays, kinetic studies by Lenzen et al. predicts that both steps influence the observed nucleotide release rate (1). (*B*) Kinetic characterization of SOS^{cat}-catalyzed nucleotide exchange assay. The nucleotide exchange assay was performed, in triplicate, in a reaction containing $KRas^{GDP}$, free MANT-GMPPNP, and an increasing concentration of SOS^{cat}. (*Upper*) Mean fluorescence values were normalized independently between 0 and 1, using the formula $Y_{normalized} = (Y_{raw} - A_0)/(M - A_0)$, where A_0 represents the fluorescence value of no SOS at 100 s, Y_{raw} is the fluorescence value of the reaction at time t, and M is the maximum fluorescence value at the end of the reaction using the highest concentration of SOS (4,000 nM). (*Lower*) Changes in fluorescence emission were fit into a single exponential association model to calculate reaction rates, which are plotted against SOS^{cat} concentration. (*C*) Kinetic characterization of SOS^{cat}-catalyzed nucleotide release assay. The nucleotide release assay was performed, in triplicate, in a reaction containing $KRas^{mant\text{-}GDP}$, unlabeled free GMPPNP, and an increasing concentration of SOS^{cat}. (*Upper*) Mean fluorescence values were normalized to no SOS control at 100 s and plotted against time. (*Lower*) Changes in fluorescence emission were fit into a single exponential decay model to calculate reaction rates, which are plotted against SOS^{cat} concentration.

1 Lenzen C, Cool RH, Prinz H, Kuhlmann J, Wittinghofer A (1998) Kinetic analysis by fluorescence of the interaction between Ras and the catalytic domain of the guanine nucleotide exchange factor Cdc25Mm. *Biochemistry* 37:7420–7430.

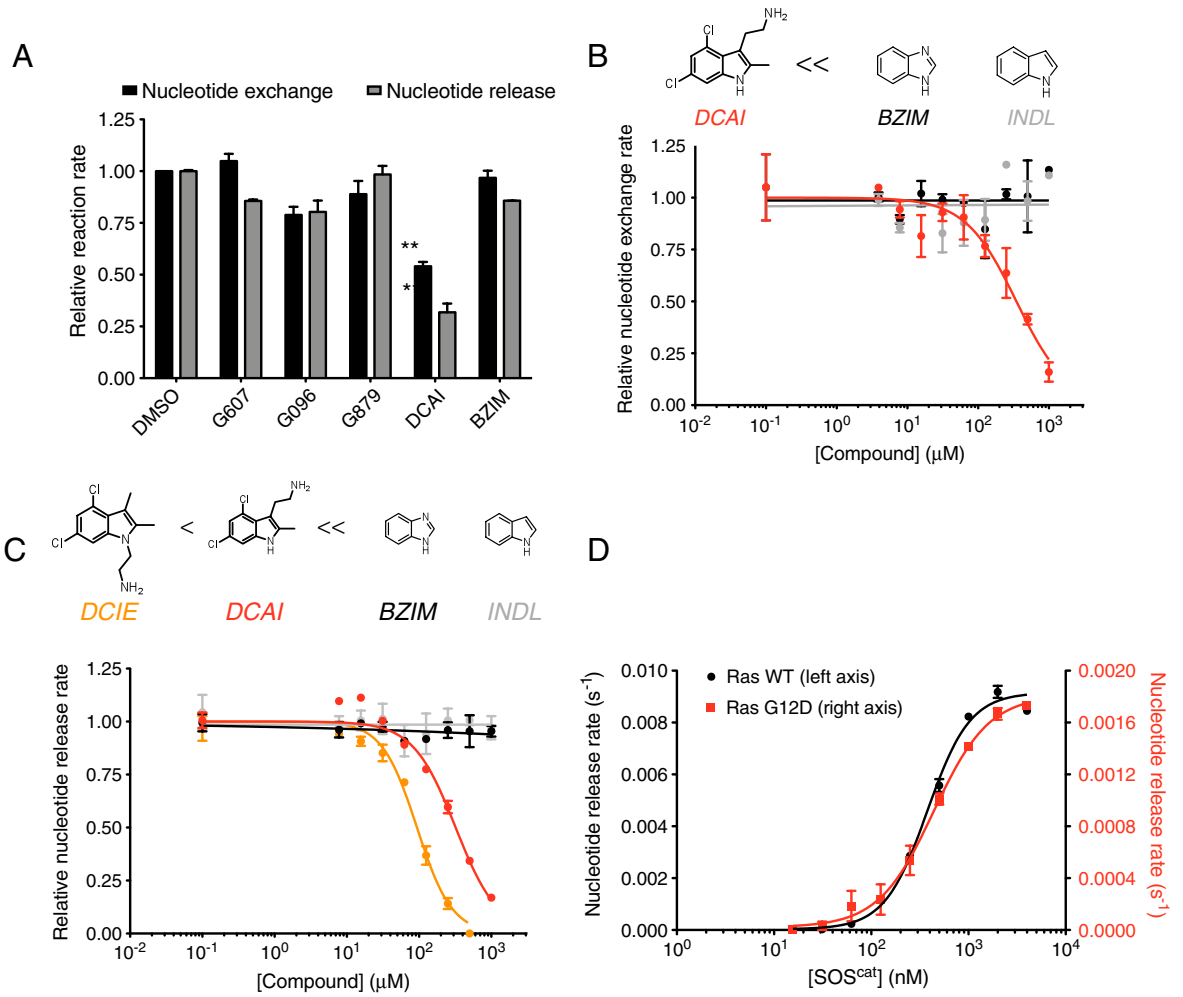

Fig. S4. Inhibition of the SOS^{cat}-catalyzed nucleotide release and exchange reactions by DCAI and 2-(4,6-dichloro-2,3-dimethyl-1H-indol-1-yl)ethanamine (DCIE). (*A*) Inhibitory effects of representative fragment hits at 500 μM were analyzed in the SOS^{cat}-catalyzed nucleotide exchange and nucleotide release assays, performed with 500 and 250 nM SOS^{cat}, respectively. The rates ($n = 3$) are plotted with values normalized to the rate of the DMSO control. **, $p < 0.005$ (Student's *t* test against DMSO control). (*B*) SOS^{cat}-catalyzed nucleotide exchange reactions were performed, in duplicate, with KRas^{GDP}, MANT-GMPPNP, and SOS^{cat} in the presence of an increasing concentration of DCAI (red), BZIM (black), or indole (INDL) (gray). Reaction rates were normalized to that of DMSO-treated sample and plotted. Average IC_{50} for DCAI over two independent experiments was 342 ± 22 μM. (*C*) SOS^{cat}-catalyzed nucleotide release assays were performed in duplicate with 125 nM SOS^{cat} in the presence of DCIE (orange), DCAI (red), BZIM (black), or INDL (gray), and the plot shows the rates normalized to that of the DMSO control. (*D*) Different catalytic efficiency of SOS on wild-type vs. mutant KRas. Nucleotide release assays were performed, in triplicate, with wild-type KRas$^{mant\text{-}GDP}$ (WT; ●, left *y* axis) or KRas$_m$mant-GDP (■, right *y* axis) across a range of SOS^{cat} concentrations. The reaction rates were plotted against SOS^{cat} concentration. Error bars in *A*–*D*, SEM.

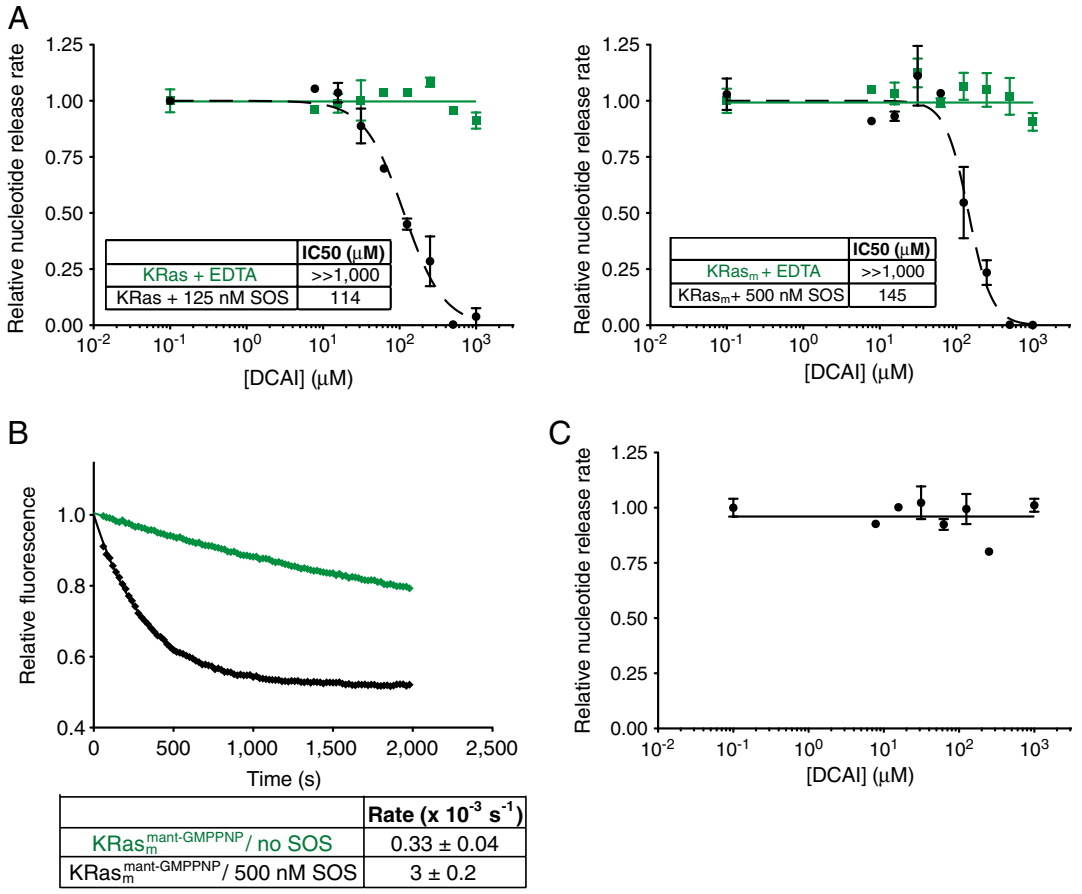

	Rate (x 10^{-3} s^{-1})
$KRas_m^{mant\text{-}GMPPNP}$ / no SOS	0.33 ± 0.04
$KRas_m^{mant\text{-}GMPPNP}$ / 500 nM SOS	3 ± 0.2

Fig. S5. SOS-dependent inhibition of nucleotide release on Ras by DCAI. (*A*) Nucleotide release assays were performed, in duplicate, with wild-type $KRas^{mant\text{-}GDP}$ (*Left*) or $KRas_m$mant-GDP (*Right*) in the presence of an increasing concentration of DCAI as indicated. The reactions were performed in the presence of unlabeled free GMPPNP, but in the absence of SOS (green curve). Nucleotide release was initiated by addition of 20 mM EDTA. As a comparison, the nucleotide release assays were also performed in the presence of SOS, but in the absence of EDTA (black curve). The reaction rates were normalized to that of the DMSO-treated sample and plotted against DCAI concentration. (*B*) Kinetic characterization of SOS^{cat}-independent nucleotide release in the absence of EDTA. This intrinsic release rate is very slow and not measurable for $KRas^{GTP}$ and $KRas^{GDP}$, but can be monitored for $KRas_m^{GMPPNP}$. The nucleotide release assay was performed, in triplicate, in a reaction containing $KRas_m^{MANT\text{-}GMPPNP}$ and unlabeled free GMPPNP in the presence (black curve) or absence (green curve) of SOS^{cat}. Mean fluorescence values are plotted against time. (*C*) Nucleotide release assays were performed, in duplicate, with $KRas_m^{MANT\text{-}GMPPNP}$ and unlabeled free GMPPNP in the presence of an increasing concentration of DCAI as indicated, but in the absence of SOS or EDTA. Changes in fluorescence emission were fit into a linear decay model to calculate reaction rates. Rates were normalized to that of DMSO control and the relative rates are plotted against DCAI concentration. Error bars in *A* and *C*, SEM.

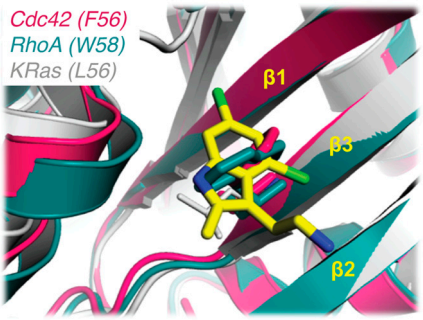

Fig. S6. Structure basis for the selectivity of DCAI on Ras vs. RhoA and Cdc42. DCAI (yellow for carbon atoms) was docked onto RhoA (cyan) and Cdc42 (magenta) structures by superimposition of the Ras coordinates (gray) from the DCAI-$KRas_m$ structure with those from RhoA [Protein Data Bank (PDB) code 1A2B] and Cdc42 (PDB code 1WMO). Trp58 from RhoA, Phe56 from Cdc42, and Leu56 from KRas are shown as sticks.

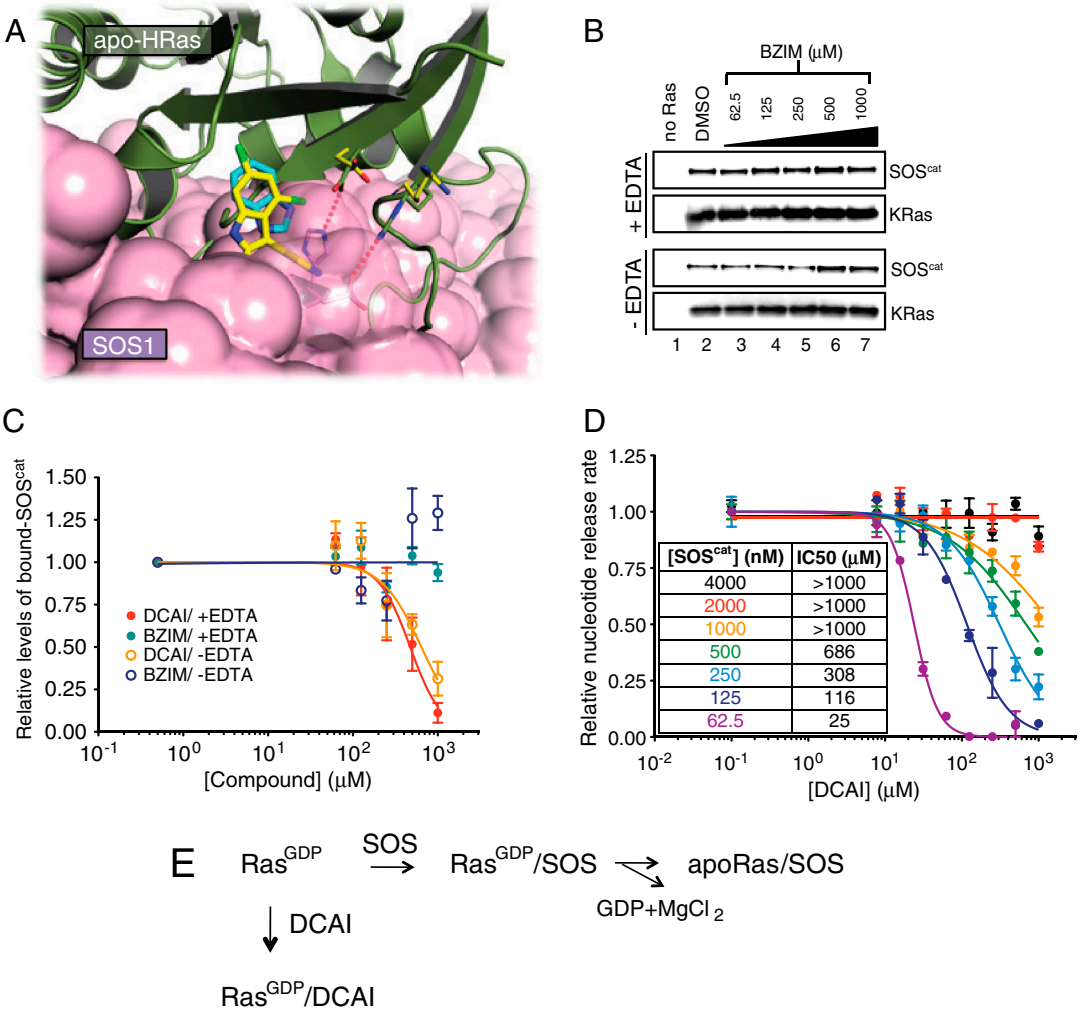

Fig. S7. DCAI is a competitive inhibitor that blocks Ras-SOS^{cat} interaction. (*A*) Ras coordinates from the DCAI-KRas$_m$ and BZIM-KRas$_m$ complexes were superimposed onto those from the HRas–SOS complex (1NVV; ref. 1; HRas bound to the substrate site of SOS) to highlight the locations of the DCAI and BZIM binding sites. The position of Ras R41 and D54 is colored in green (for carbons) in the Ras–SOS complex and in yellow (for carbons) in the Ras–DCAI complex. (*B*) (*Top*) Nucleotide-free biotinylated KRas was generated by incubation with EDTA. Streptavidin beads were incubated with SOS^{cat} alone (lane 1; negative control) or with SOS^{cat} plus nucleotide-free biotinylated KRas in the presence of increasing concentrations of BZIM (lanes 3–7). Bead-associated SOS^{cat} was purified, washed, and detected by Western blotting. (*Bottom*) Identical reactions as above, with the exception that EDTA was omitted in the reaction. Results shown are representative of three independent experiments. (*C*) Quantification of experiments in Fig. 4*C* and Fig. S7*B*. The amounts of bead-bound SOS^{cat} in Fig. 4*C* and Fig. S7*B* were quantified by Western blotting using an infrared imaging system, normalized to those of DMSO-treated samples, and plotted against DCAI concentration. (*D*) Nucleotide release assays were performed, in duplicate, with a dose titration of DCAI across a range of SOS^{cat} concentrations. The reaction rates were normalized to those of DMSO control and plotted for each concentration of SOS^{cat}. Error bars in *C* and *D*, SEM. (*E*) Mechanism of DCAI function.

1 Margarit SM, et al. (2003) Structural evidence for feedback activation by Ras. GTP of the Ras-specific nucleotide exchange factor SOS. *Cell* 112:685–695.

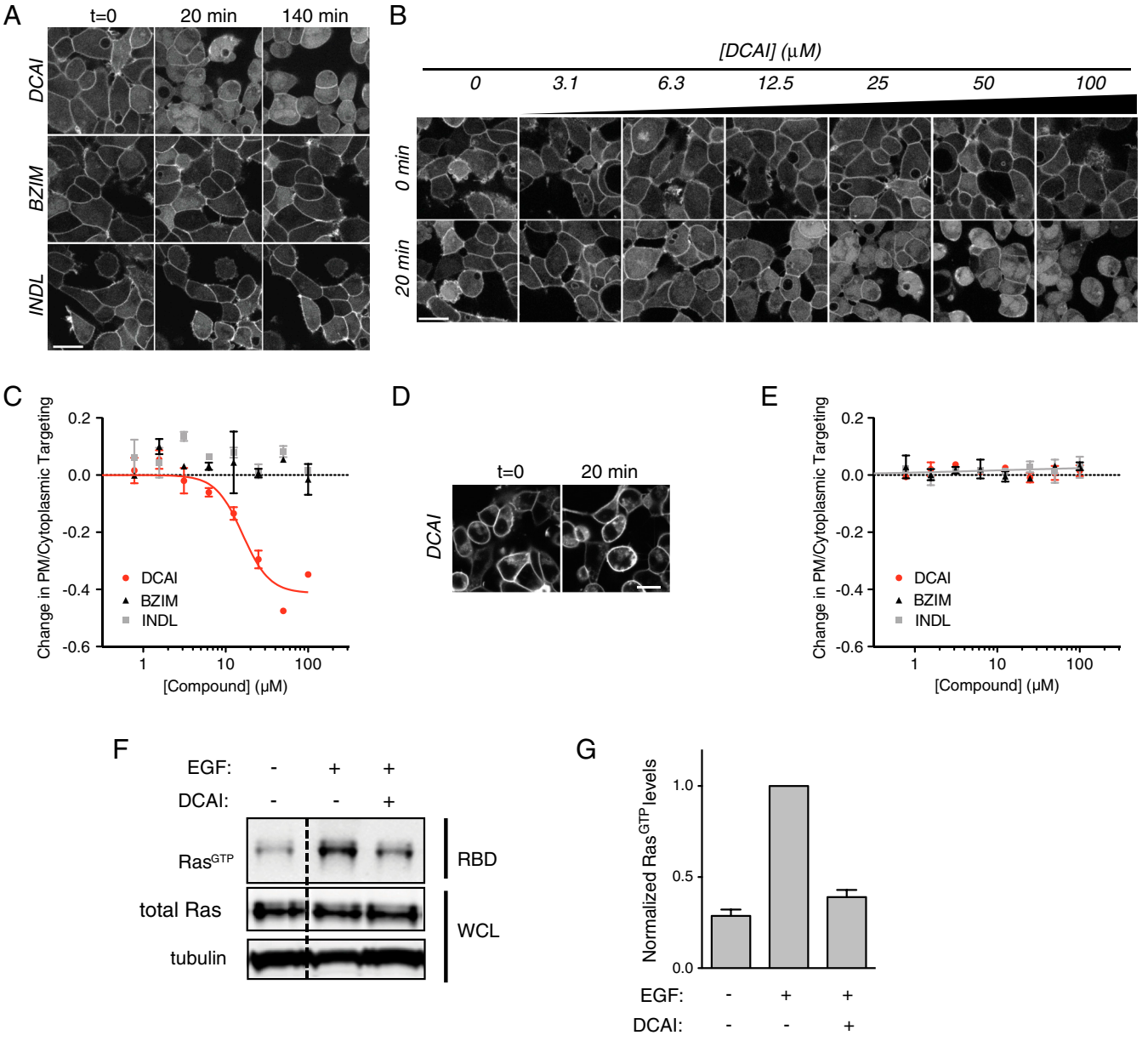

Fig. S8. DCAI inhibits Ras activation in HEK-293T cells. (*A*) Images of HEK 293 T-REx Flp-In cells expressing Venus-RBD-CRD treated with 25 μM of DCAI, BZIM, or indole (INDL) and imaged at 0, 20, and 140 min after compound addition. (*B*) Images of HEK 293 T-REx Flp-In cells expressing Venus-RBD-CRD treated with an increasing dose of DCAI and imaged at 0 and 20 min after compound addition. (*C*) HEK 293 T-REx Flp-In cells expressing Venus-RBD-CRD were treated with an increasing dose of DCAI (red), BZIM (black), or INDL (gray) and imaged live. The targeting ratio of RBD-CRD at the plasma membrane (PM) vs. the cytoplasm was normalized to that of DMSO control, subtracted from time zero, and then fit to a sigmoidal curve. We determined that the cellular concentrations of SOS1 and Ras in HEK 293T cells are 5 and 350 nM, respectively. In HEK-293T cells, the EC_{50} of DCAI in this assay is at 15.8 ± 0.4 μM, consistent with the inhibitory potency of DCAI in the in vitro nucleotide release assay (Fig. S7*D*). At 62.5 nM of SOS^{cat} and 125 nM of Ras, the IC_{50} value of DCAI is 25 μM (Fig. S7*D*). (*D*) Images of HEK 293 T-REx Flp-In cells expressing eCFP-$KRas_m$ treated with 25 μM of DCAI and imaged at 0 and 20 min after compound addition. (Scale bars in *A*, *B*, and *D*: 20 μm.) (*E*) HEK 293 T-REx Flp-In cells expressing Venus-Smad-7 and eCFP-Smurf-1 were treated with an increasing dose of DCAI (red), BZIM (black), or INDL (gray) and Smad-7 PM targeting was analyzed as in (*C*). Results shown in *C* and *E* are representative of three independent experiments. (*F*) DCAI reduces EGF-stimulated Ras^{GTP} levels in HEK 293T cells. HEK 293T cells were serum-starved for 16 h, treated with DMSO or 100 μM DCAI for 2 h, stimulated with EGF for 5 min and then lysed. The levels of endogenous Ras^{GTP} was determined in a GST-RBD effector pull-down assay followed by Western blotting with an anti-pan-Ras antibody. RBD, Ras-binding domain from cRaf protein; WCL, whole cell lysates. (*G*) Quantification for the effect of DCAI on Ras^{GTP} levels in HEK 293 cells. Experiments described in *F* were performed three times and the amounts of bead-bound RasGTP were quantified using an infrared imaging system, normalized to those of DMSO-treated samples, and plotted. Error bars *C*, *E*, and *G*, SEM.

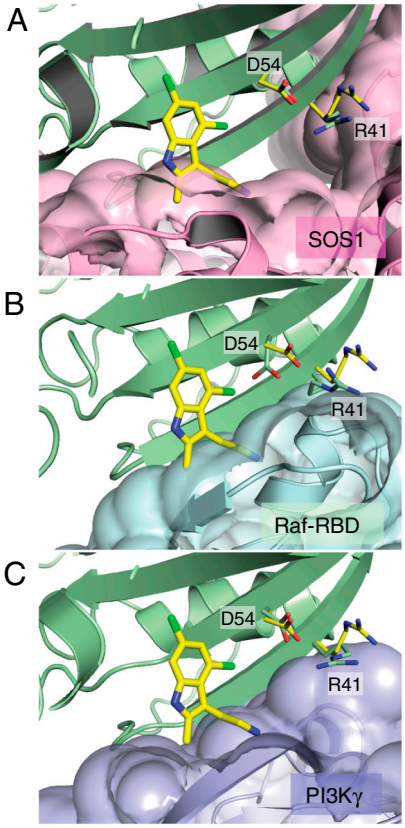

Fig. S9. DCAI does not appear to interfere with the binding of Ras to Raf, to PI3Kγ, or to the allosteric site in SOS^{cat}. (*A*) A docking model of DCAI binding to Ras at the allosteric site in SOS^{cat}. The model was generated by superimposing the DCAI-$KRas_m$ coupled onto the HRas–SOS complex [Protein Data Bank (PBD) 1NVV] (1). The carbon atoms of Ras and D54 are colored in green in the Ras–SOS complex and in yellow in the DCAI–Ras complex. This study analyzes the effect of DCAI on allosteric activation. Although Ras R41 and D54 are critical for Ra/SOS interactions at the catalytic site (Fig. 4*A* and Fig. S7*A*), they are not involved in direct interactions with SOS at the allosteric site. Furthermore, DCAI binding at the allosteric sith constitutes no or minimal steric hindrance for the/SOS interaction. (*B*) A docking model of DCAI binding to Ras-RBD (from cRaf) interface. The model was generated by superimposing the DCAI-$KRas_m$ complex onto the Ras–RBD complex (PBD 3KUD) (2). The carbon atoms of Ras and D54 are colored in green in the Ras-RBD complex and in yellow in the DCAI-Ras complex. (*C*) A docking model of DCAI binding to the Ras-P13Kγ complex (PBD-1HE8) (3). The carbon atoms of Ras R41 and D54 are colored in green in the Ras-P13Kγ complex and in the DCAI-Ras complex. In A-C, Ras R41, and D54 do not appear to be involved in complex formation. Although DCAI may not directly affect Ras-effector interaction or allosteric activation of SOS, we speculate that DCAI derivatives with bulky substitutes may inhibit Ras-effector signaling and allosteric activation of SOS as the DCAI binding pocket is at the interface of these complexes.

1 Margarit SM, et al. (2003) Structural evidence for feedback activation by Ras. GTP of the Ras-specific nucleotide exchange factor SOS. *Cell* 112:685–695.
2 Filchtinski D, et al. (2010) What makes Ras an efficient molecular switch: A computational, biophysical, and structural study of Ras–GDP interactions with mutants of Raf. *J Mol Biol* 399:422–435.
3 Pacold ME, et al. (2000) Crystal structure and functional analysis of Ras binding to its effector phosphoinositide 3-kinase gamma. *Cell* 103:931–943

Table S1. X-ray data collection and refinement statistics

	KRas4B G12D–GTPγS–BZDN	KRas4B G12D–GDP–DCAI	KRas4B G12D–GDP–BZIM
Data collection			
X-ray source/detector	SSRL11-1/MAR 325	ALS502/ADSC Q315	ALS502/ADSC Q315
Resolution, Å	30–1.92	30–2.30	50–1.70
Total no. of reflections	73,756	40,500	93,984
R_{sym}*	0.059 (0.158)	0.092 (0.332)	0.046 (0.455)
Completeness	98.7 (89.7)	94.5 (70.8)	99.9 (100)
Redundancy	5.3 (4.4)	5.2 (3.3)	4.6 (4.6)
I/σ	18.1 (7.4)	18.0 (3.0)	26.7 (3.2)
Refinement			
Resolution range, Å	30–1.92	50–2.30	30–1.70
R_{cryst}‡ /R_{free} §	0.181/0.216	0.166/0.223	0.160/0.203
Non-hydrogen atoms	1,594	1,590	1,489
Average B, overall	30.7	40.8	43.7
Protein	30.5	40.8	43.9
Solvent	34.8	40.7	46.7
Rmsd bond lengths, Å	0.008	0.005	0.006
Rmsd angles	1.302°	1.005°	0.959°
Ramachandran (C/A/G/D)¶	87.1/8.6/3.1/1.2	90.8/8.0/0.0/1.2	89.9/7.0/2.5/0.6

Space group R3, unit cell $a = b = 79$ Å, $c = 77$ Å, $\alpha = 90°$ $\beta = 120°$ $\gamma = 90°$.

*$R_{sym} = \sum_h |I_{hi}\text{-}I_h| / SI_{hi}$, where I_{hi} is the scaled intensity of the ith symmetry-related observation of reflection h and I_h is the mean value.

†Values in parentheses are of the highest resolution shell.

‡$R_{cryst} = \sum_h |F_{oh}\text{-}F_{ch}| / S_h F_{oh}$, where F_{oh} and F_{ch} are the observed and calculated structure factor amplitudes for reflection h.

§Value of R_{free} is calculated for 5% randomly chosen reflections not included in the refinement.

¶Ramachandran plot regions: C, core; A, allowed; G, generally allowed; D, disallowed. Numbers indicate percentage of residues.